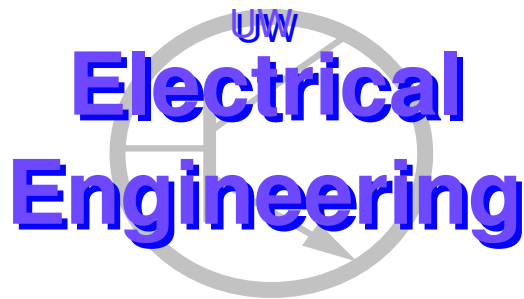

Multichannel Equalization by Decision-Directed Passive Phase Conjugation: Experimental Results

John A. Flynn , James A. Ritcey , Daniel Rouseff , and Warren L. J. Fox

*Department of Electrical Engineering
University of Washington*

and

*Applied Physics Laboratory
College of Ocean and Fishery Sciences
University of Washington
1013 NE 40th St.
Seattle, WA 98105*



UWEE Technical Report
Number UWEETR-2004-0002
January 2004

Department of Electrical Engineering
University of Washington
Box 352500
Seattle, Washington 98195-2500
PHN: (206) 543-2150
FAX: (206) 543-3842
URL: <http://www.ee.washington.edu>

Multichannel Equalization by Decision-Directed Passive Phase Conjugation: Experimental Results

John A. Flynn , James A. Ritcey , Daniel Rouseff , and Warren L. J. Fox

Department of Electrical Engineering
University of Washington

and

Applied Physics Laboratory
College of Ocean and Fishery Sciences
University of Washington
1013 NE 40th St.
Seattle, WA 98105

University of Washington, Dept. of EE, UWEETR-2004-0002

January 2004

Abstract

An adaptive technique for underwater acoustic communication using passive phase conjugation (PPC) is developed. Multipath channel parameter identification is accomplished by decision-directed model building and finite-window, block-updated least-squares computed by LSQR (an iterative linear systems solver). The resulting channel estimates are then used by the PPC processor to generate decisions for use in the next processing block. This architecture effectively accomplishes array equalization with low computation cost in shallow water environments that exhibit rapidly fluctuating multipath scattering. Performance on shallow-water acoustic communications channels is demonstrated at ranges of 0.9 to 4.6 km under windy surface conditions and shipping noise, using measured wide-band telemetry data with BPSK signaling. The algorithm is evaluated with sparse receiver apertures using subsets of a 14-element array.

1 Introduction

Underwater acoustic communication is hampered by the time- and frequency-spread inherent to propagation through the ocean. Coherent communications algorithms often attempt to track these changes and compensate using an adaptive equalizer [1, 2, 3]. These systems typically employ recursive least squares (RLS) algorithms and seek to approximately invert the channel and remove intersymbol interference. Many current approaches suffer from well-known difficulties when applied to multichannel receiving arrays. This problem is of high dimensionality, the channel dynamics can vary rapidly, and the received data can be very noisy. Standard RLS algorithms employ exponential error weighting and so have difficulty reacting rapidly in nonstationary environments, in contrast to block or finite-window based algorithms. As a result RLS can be prone to catastrophic failure (loss of lock) when applied to underwater acoustic telemetry. Further, the high dimensionality of the problem contributes to both ill-conditioning and extreme computational complexity.

In the present paper, we develop an alternative approach that we call Decision-Directed Passive Phase Conjugation (DDPPC). The method uses multiple hydrophones (channels) with a matched filter for each. The matched filters are derived from the in-situ measurements; a physics-based model for the channel is not required. The symbol estimates from the combined processor that uses all the hydrophones are used in a feedback loop to update each of the matched

filters adaptively. The updated matched filters are calculated in parallel on each channel thereby improving efficiency, reducing the parameter search space, and enhancing stability. By using multiple hydrophones and adaptive matched filters rather than equalizers, we circumvent the inverse problem. The multiple hydrophones provide both the usual spatial coherent gain against noise and directional interference, and sufficient diversity to equalize multipath. This last property is an outgrowth of matched filtering in an environment that acts as a waveguide [4]. Our approach seeks to produce an effective space–time (multi–channel) equalizer, one of the critical problems in underwater acoustic communication [5].

Passive Phase Conjugation (PPC) has its origins in the physics of acoustic propagation in a waveguide. In active phase conjugation, a source transmits a signal that is measured along an array. The measurement is then rebroadcast from the array but in a time–reversed (“phase conjugate”) fashion. The backpropagated field focuses back at the location of the original source. A key point is that the focus is actually sharper in a waveguide than it would be in free–space; one can show that all the multipaths in the waveguide add together in phase at the focus. Jackson and Dowling [6] first proposed active phase conjugation for use in the ocean waveguide and Kuperman *et al.*[7] subsequently demonstrated it in an experiment in the Mediterranean. Dowling [4] used reciprocity to show how analogous pulse compression could be achieved using a receive–only array. He further suggested that this passive version of phase conjugation could be used for underwater communication. Silva *et al.*[8] independently proposed PPC and tested it in numerical simulations. Athanasiou [9] studied communication using both active and passive phase conjugation in laboratory experiments. As part of the SignalEx experiments [10], Hursky *et al.*[11] demonstrated PPC with a single receiving hydrophone for a low–power, low data–rate application. Finally, Rouseff *et al.*[12] used a 14–element receiving array in a PPC communications experiment in Puget Sound.

In the examples of passive phase conjugation cited above, simply sending a probe pulse and measuring the response supplied the necessary matched filters. To compensate for a changing environment, fresh estimates for the matched filter coefficients are typically obtained by interspersing new probe pulses into an extended telemetry stream. This approach has the virtue of simplicity, but is inefficient. In the decision–directed version of PPC described in this paper, the demodulator output is quantized to give tentative symbol estimates that are then fed back into a channel estimation algorithm [13], [14]. The channel estimation produces the matched filter coefficients needed by the PPC processor for the next processing block, and are obtained by least squares identification of a single–input/multiple–output (SIMO) system formulated into Q independent linear statistical models, where Q is the number of sensor channels. The initial estimation employs a known training data preamble. Subsequent channel estimates result from iterations of an LSQR algorithm [15] applied to the SIMO linear model after it has been updated with the most recent block of tentative symbol estimates. At each block, the LSQR algorithm uses the previous block’s channel estimate as an initial guess at solving the current block’s normal equations. In contrast with many other multi–channel equalizers [16], no direct error signal feedback is used, so optimization is partitioned across sensor channels as distinct estimation problems rather than jointly over all channels. The scheme gives efficient, robust, block–updated, uniformly–weighted LS estimation, with complexity scaling linearly in Q . These features should provide an attractive alternative to exponentially–weighted RLS when attempting to track noisy channels having significant Doppler spread.

In Sections 2 and 3, we develop the signal models and describe the Decision–Directed Passive Phase Conjugation algorithm. In Section 4, we apply the algorithm to data taken in a previous field experiment [12]. We show how the LSQR procedure typically converges after only two iterations making the overall algorithm fast. We present performance results where subsets of the full 14–element array are used. Examples are shown of the channel impulse response, an interesting byproduct of the communications algorithm. Discussion and suggestions for future research are in Section 5.

Table 1 describes principal variables in the paper. Bold font indicates vector- or matrix-valued variable. Estimates of quantities are indicated by the circumflex “ $\hat{}$ ” symbol. The term CIR abbreviates “channel impulse response”.

2 Signal Models

In this section signal models are defined. We assume symbol–rate processing throughout the mathematical developments, where the independent time variable t indicates integer sample times corresponding to normalized sampling frequency $\omega/(2\pi F_s)$.

The transmitted information symbol stream is the serialized data packet $\{I_k\}_0^{N_s-1}$ containing N_s symbols under

BPSK signaling so that so $I_k \in \{-1, +1\}$. Then the baseband transmit signal is

$$x(t) = \sum_{k=0}^{N_s-1} I_k f_{t-k} = \sum_{k=t-N_s+1}^t f_k I_{t-k}, \quad (1)$$

where f_k is the transmit pulse sampled at times k . The symbols I_k are considered uncorrelated random variables with zero mean.

2.1 Time invariant channel

After propagation through the ocean acoustic channel, a model for the baseband signal (within a bulk delay common to all channels) recorded by sensor q , $q \in \{1, \dots, Q\}$ is

$$y^q(t) = \sum_l \alpha_l^q x(t - D_l^q) + v_{amb}^q(t), \quad (2)$$

where the numerous path attenuations α_l^q are complex, and the D_l^q terms represent path delays. $v_{amb}^q(t)$ is zero-mean environment and sensor noise that is space-time uncorrelated. Initially to illustrate the basic PPC concept we approximate the baseband-equivalent channel signal at sensor q using a moving-average model, with impulse response truncated to L coefficients. The expression for the signal observed by sensor q is then

$$y^q(t) = \sum_{l=0}^{L-1} h^q(l) I_{t-l} + v_{amb}^q(t). \quad (3)$$

where L is the length of the modeled channel impulse response (CIR) in samples. For convenience the transmit pulse shape f_k is lumped into the physical CIR $h^q(l)$.

2.2 Time-varying channel and approximation

In the following we expand the channel model to help illustrate the DDPPC algorithm's tracking behavior and the approximations made in its development. Here the discrete scattering model (2) is modified to acknowledge time-varying channel behavior by allowing path delays D_j^q and path gains α_j^q to be functions of time rather than constant. We model this system with a time-varying impulse response, then simplify using a piecewise-fixed impulse response description for representing identifiable parameters.

For mathematical developments that use the time-varying channel model, it is convenient to partition the time index into blocks. We use $\tau = \tau(t)$ to indicate sample times constrained to a processing block interval, and t as the block's time-index as follows. Writing the q^{th} sensor signal $y^q(t, \tau) = y^q(\tau)$ on processing block t as the output of a time-varying system at times $\tau \in \mathcal{T}_t$, $\mathcal{T}_t = \{t - N + 1, \dots, t\}$ gives

$$y^q(\tau) = \sum_{l=0}^{\infty} h^q(\tau, l) I_{\tau-l} + v_{amb}^q(\tau), \quad (4)$$

where $h^q(\tau, l)$ is the response of channel q at time $\tau + l$ to an impulse presented at time τ . Approximating $h^q(\tau, l)$ with a piecewise-constant impulse response for each block t , we get

$$y^q(\tau) = \sum_{l=0}^{L-1} h_t^q(l) I_{\tau-l} + v^q(t, \tau), \quad (5)$$

where $h_t^q(l)$ is a truncated nominal impulse response that is time-invariant on the block interval \mathcal{T}_t . Associated with $h_t^q(l)$ is $\Delta h_t^q(\tau, l)$, its implied modeling error over the block. The total error signal segment on \mathcal{T}_t is then

$$v^q(t, \tau) = v_{rev}^q(\tau) + v_{tw}^q(t, \tau) + v_{amb}^q(\tau), \quad (6)$$

where $v_{rev}^q(\tau)$ denotes the *reverberation* signal

$$v_{rev}^q(\tau) = \sum_{l=L}^{\infty} h^q(\tau, l) I_{\tau-l}, \quad (7)$$

and $v_{tv}^q(t, \tau)$ denotes the *time-varying model error* (TVME), defined as

$$v_{tv}^q(t, \tau) = \sum_{l=0}^{L-1} \Delta h_t^q(\tau, l) I_{\tau-l}. \quad (8)$$

Note that the TVME, $v_{tv}^q(t, \tau)$, is not necessarily unique in τ . Depending on the block increment M and observation size N , adjacent segments $v_{tv}^q(t_A, \tau)$ and $v_{tv}^q(t_B, \tau)$ for successive processing block indices t_A and $t_B = t_A + M$ may have overlapping time supports \mathcal{T}_{t_A} and \mathcal{T}_{t_B} ; however, the values of $v_{tv}^q(t_A, \tau)$ and $v_{tv}^q(t_B, \tau)$ will not in general be identical.

In the error decomposition (6), we interpret reverberation to be a property of the channel, in the same sense as ambient noise. The values of $h^q(t, l)$ for $l \geq L$, the components truncated from the modeled impulse response, are assumed to be so rapidly varying in t that attempts to estimate them would be fruitless. This assumption supports a stochastic interpretation for the truncated impulse response components. However, we interpret the TVME component not as a noise source intrinsic to the channel, but as a product of the compromise made by the model (5) in obtaining a piecewise-invariant CIR. Consequently it is a shortcoming of the LS channel estimation structure that will be derived from (5) in Section 3.2.1. Discussion in Section 4.2 will clarify this distinction and its importance to channel SNR estimation.

3 Algorithm Description

This section describes the basic PPC array equalization concept from [12]. The decision-directed channel estimation formulation and its fast execution by LSQR are then outlined. The basic PPC algorithm is then integrated into the adaptive structure, and algorithm pseudocode is presented.

3.1 Multichannel Equalization by Passive Phase Conjugation

Here we review the basic PPC array demodulation concept introduced in [12] for convenience and notational consistency. We present a brief discussion of its equalizing behavior in the context of fixed channels. For clarity the block processing concept is not used here, so t represents an ordinary time index as in Section 2.1.

The PPC algorithm processes multiple time series acquired by an array of hydrophones that are sampling the local acoustic field due to a distant acoustic transmitter. The PPC demodulator output signal $r(t)$ evaluated at symbol intervals approximates the transmitted source symbol stream $\{I_t\}$, so that ISI effects due to the acoustic channel's multipath and delay spread are effectively mitigated. This allows a memoryless decision device or quantizer to then infer the symbol stream $\{I_t\}$ values from $r(t)$.

The PPC concept is simple: it is basically a set of filters matched to the sensor CIRs followed by a memoryless spatial combiner. A caveat is that relative bulk delay must be preserved among the matched filters of the Q sensor channels. Under the fixed channel model (3) the PPC demodulator [12] is the sum of matched-filter outputs z^q

$$r(t) = \sum_{q=1}^Q z^q(t), \quad (9)$$

where the correlations $z^q(t)$ are

$$\begin{aligned} z^q(t) &= \sum_{l=0}^{L-1} h^{q*}(l) y^q(t+l) \\ &= \sum_{l=0}^{L-1} h^{q*}(l) \cdot \\ &\quad \left[\sum_{k=0}^{N_s-1} h^q(t+l-k) I_k + v_{amb}^q(t+l) \right]. \end{aligned} \quad (10)$$

Equivalently,

$$z^q(t) = \sum_{l=-L+1}^{L-1} \rho_l^q I_{t-l} + w^q(t), \quad (11)$$

where ρ_l^q is the deterministic autocorrelation of the CIR $h^q(t)$, and $w^q(t)$ is noise at the matched filter outputs. The CIR vectors, denoted by \mathbf{h}_l^q for the q^{th} channel, are unknown to the receiver and must be estimated.

The equalizing behavior of the PPC algorithm was first noted in the underwater acoustic context in [4]. Here we explain this behavior by heuristic reasoning, although a stronger conclusion results from a modal decomposition argument for phase conjugation in a waveguide [6], [12]. Combining eqns. (9) and (11) gives

$$r(t) = \sum_{l=-L+1}^{L-1} I_{t-l} \bar{\rho}_l + \bar{w}(t), \quad (12)$$

where the coherent sum $\bar{\rho}_l$ defines the total system impulse response (of length $2L - 1$) from source to $r(t)$. In $\bar{\rho}_0$ the zero-lags of the individual matched-filter responses $\rho_l^q|_{l=0}$ of (11) are summed in-phase, since by a property of autocorrelation functions the ρ_0^q must be real. However, because the multipath nature of the shallow-water channel induces a dispersed angular spectrum of the field at the array, at nonzero lags l the complex ρ_l^q are likely distinct among q and tend to combine destructively. Thus the peak distortion measure [17] of $\bar{\rho}_l$ is improved over that of individual ρ_l^q , and a memoryless quantizer can estimate symbol \hat{I}_k from samples of $r(t)$. This heuristic argument appears earlier, for example in the context of the matched-filtering components of a multichannel equalizer [18]. The space-time matched-filter architecture has been used as an economical array combining technique in terrestrial wireless communications. For example, Liu [19, p. 86] discusses its use and limitations in conjunction with spread-spectrum modulation, although not specifically in a waveguide propagation environment.

3.2 Decision-Directed Adaptation: DDPPC

Here we motivate and describe the decision-directed extension to PPC, which we call DDPPC. This adaptation mechanism addresses the estimation of CIRs in a changing acoustic environment, enabling robust operation without repeated acoustic channel probing.

To illustrate the need for frequent adaptation in some environments, we compare the demodulator output of a 14-channel PPC receiver structure without adaptation (training by only an initial probe), and with block-adaptation at a rate on the order of the CIR length. The comparison is demonstrated in Fig. 1 on the experimental data set \mathcal{C} (described in Section 4.1). The plot clearly shows almost complete mismatch of the PPC filters after about 1/2s, while the decision-directed estimator tracks throughout the entire packet.

As illustrated in Fig. 2 (diagram taken from [14]), DDPPC generates least-squares estimates (LSE) of each channel's CIR. Each LSE computation uses the most recent set of $(N + L - 1)$ symbol estimates and N corresponding sensor observations $y^q(\tau)$ in a block-updated fashion. Then the set of Q CIR estimate vectors are taken as their predicted values for M "update" symbol periods into the future, so they may be used to approximate the matched-filtering operation (10), which forms the soft-demodulation decision metric (9). The decision metric r is then corrected for any residual bulk phase error and quantized, giving the next batch of M inferred symbol estimates. The algorithm's architecture is illustrated in Fig. 2. Downconverter filters (not shown) have the outputs $y^1 \dots y^Q$ in Fig. 2.

3.2.1 Channel Estimation

For CIR estimation, we choose a linear statistical model formulation with a finite observation window and uniform weighting. This limits the time over which modeling error is allowed to grow, but makes equal use of all observations to minimize estimate error variance. In contrast both LMS and exponentially-weighted RLS algorithms, while numerically efficient for estimation, often suffer from a poor design tradeoff regime when operating in the shallow-water acoustic environment. Simultaneous reduction of both estimation error due to observation noise (reduced by a larger forgetting factor) and modeling error due to time-varying multipath parameters (reduced by a smaller forgetting factor) is frustrated by effects of surface winds, relative platform motion, reverberation, and prominent environmental noise. It is well known that the LSE for deterministic parameters in the linear model is also the best linear unbiased estimator for a given observation size, assuming white observation noise [20].

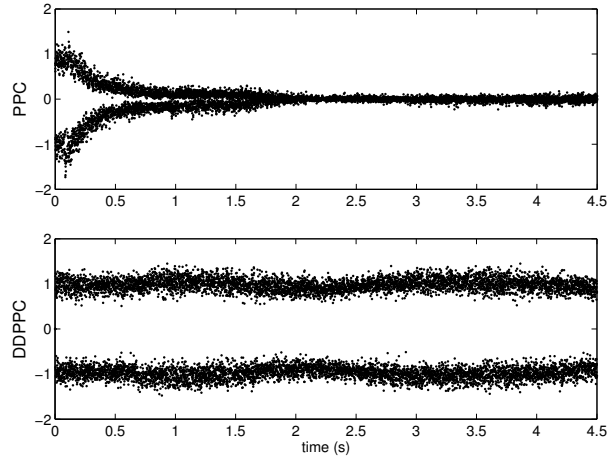


Figure 1: Comparison of PPC with and without decision-directed adaptation. Upper panel shows PPC demodulator output using CIR estimation only at beginning of packet. Lower panel shows PPC output with decision-directed estimation updated approximately once every impulse response length. Decision direction requires no recurring training cost. From data set \mathcal{A} .

In the following we give details of the CIR estimation algorithm employed by DDPPC, represented by the box labeled “LSE” in Fig. 2. This formulation starts from a straightforward generalization of the single-sensor least-squares (LS) data-aided channel estimation problem [21] to the SIMO multichannel case. Uncorrelated noise assumptions then decomposes this into Q separate single-channel LS estimation problems. A fast method of computation is described in a later section.

First we define the CIR, observation, and noise vectors respectively as

$$\mathbf{h}_t^q = [h_t^q(0), \dots, h_t^q(L-1)]^T \sim (L \times 1), \quad (13)$$

$$\mathbf{y}_t^q = [y^q(t-N+1), \dots, y^q(t)]^T \sim (N \times 1), \quad (14)$$

$$\mathbf{v}_t^q = [v^q(t-N+1), \dots, v^q(t)]^T \sim (N \times 1), \quad (15)$$

and the $(N \times L)$ Toeplitz-structured convolution matrix of past symbols as

$$\mathbf{X}_t = \begin{pmatrix} I_{t-N+1} & \cdots & I_{t-N-L+2} \\ \vdots & & \vdots \\ I_t & \cdots & I_{t-L+1} \end{pmatrix}. \quad (16)$$

This permits the following linear statistical model description for the array observations (5) in vector-matrix format

$$\mathbf{Y}_t = (\mathbf{I}_Q \otimes \mathbf{X}_t) \mathbf{H}_t + \mathbf{V}_t, \quad (17)$$

where \mathbf{I}_Q is the $(Q \times Q)$ identity matrix, \mathbf{Y}_t is the $(NQ \times 1)$ supervector $[y_t^1; \dots; y_t^Q]$ of stacked observations, \mathbf{V}_t is defined similarly from the observation error vectors \mathbf{v}_t^q , $\mathbf{H}_t = [\mathbf{h}_t^1; \dots; \mathbf{h}_t^Q] \sim (LQ \times 1)$, and \otimes is the Kronecker product [20]. We interpret errors \mathbf{V}_t as being random and zero mean, so $E[\mathbf{Y}_t | \mathbf{X}_t, \mathbf{H}_t] = (\mathbf{I}_Q \otimes \mathbf{X}_t) \mathbf{H}_t$. Assuming spatially uncorrelated errors, the covariance $E\{\mathbf{V}_t \mathbf{V}_t^T\}$ has block diagonal form. Further, the $(N \times L)$ column partitions of $\mathbf{I}_Q \otimes \mathbf{X}_t$ are orthogonal due to its block-diagonal structure. These two conditions permit a simplification [22] that decomposes the parameter estimation problem for (17) into the Q independent linear models

$$\mathbf{y}_t^q = \mathbf{X}_t \mathbf{h}_t^q + \mathbf{v}_t^q, \quad (18)$$

as depicted in Fig. 2. Further simplifying to the temporal white noise model

$$\text{cov}(\mathbf{v}_t^q) = \sigma_v^{q2} \mathbf{I}_N \quad (19)$$

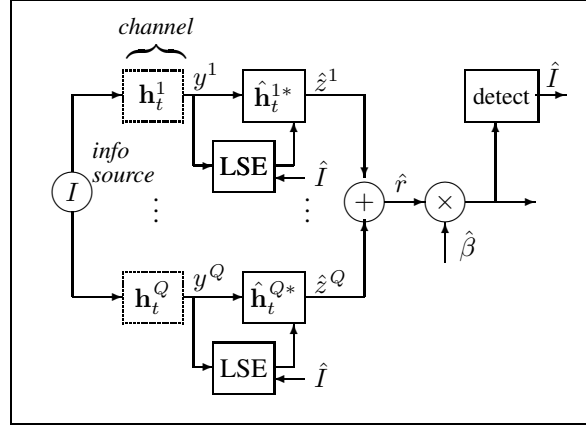


Figure 2: Baseband-equivalent DDPPC architecture for MPSK modulation. Channel noise and downconversion filtering not shown.

yields the channel q impulse response LSE

$$\hat{\mathbf{h}}_t^q = \underset{\mathbf{h}_t^q}{\operatorname{argmin}} \|\mathbf{y}_t^q - \mathbf{X}_t \mathbf{h}_t^q\|^2, \quad (20)$$

which solves the q^{th} set of normal equations $\mathbf{X}_t' \mathbf{X}_t \hat{\mathbf{h}}_t^q = \mathbf{X}_t' \mathbf{y}_t^q$. The LSE $\hat{\mathbf{h}}_t^q$ by linear model theory is also the best linear unbiased estimate. For it to be unique it is necessary that $N \geq L$, but generally we have $N \gg L$ to combat noise and reduce the possibility of rank-deficiency in \mathbf{X}_t .

If previous symbol detection errors in the construction of \mathbf{X}_t can be neglected, the temporal whiteness assumption (19) in practice seems reasonable if the downconversion filter and transmit spectrum are flat over the baseband sampling bandwidth and errors are dominated by lengthy, overspread reverberation. However, in processing our experimental data we violate these conditions due to the shaped transmit pulse spectrum and the resulting colored noise from reverberation. Nonetheless we employ the white noise model and avoid the complexity of a generalized linear model. We justify the spatial whiteness approximation by the fact that the vertical array sparsely samples the aperture in our experimental set-up, where element spacing is on the order of 15 wavelengths. This allows great complexity reduction in the multichannel CIR estimation problem.

At time t_0 of the first estimation block, the minimization (20) uses an \mathbf{X}_{t_0} filled with a transmitted training sequence of N_{train} symbols that constitute a packet preamble known at both source and receiver. Here $t_0 = N_{\text{train}} - 1$ where $N_{\text{train}} = N + L - 1$. The solution for $\hat{\mathbf{h}}_{t_0}^q$ can be aided by precomputation based on the known training sequence, e.g. by using a stored decomposition of \mathbf{X}_{t_0} . For subsequent block times $t > t_0$, \mathbf{X}_t is defined by decision direction using past symbol estimates, as shown in Fig. 2 by the ‘‘LSE’’ component’s input labeled \hat{I}_k . During these estimation blocks, (20) is solved by a fast iterative method described later.

3.2.2 Fast Estimate Computation

Direct solution of (20), though acceptable for training, would be prohibitively expensive to employ during every subsequent processing block of a packet. We choose to employ the LSQR algorithm [15] to solve for the CIR parameter vectors $\hat{\mathbf{h}}_t^q$ in (20). LSQR is an iterative method for solving overdetermined systems of linear equations. We avoid analysis of the LSQR algorithm here, but address the mechanics of its application to our problem, as follows.

Applying PPC filtering (as detailed in Section 3.2.3) with the Q CIR estimates $\hat{\mathbf{h}}_t^q$ generates M symbol detections $\hat{I}_\tau, \tau \in \mathcal{M}_t$. The *update interval* \mathcal{M}_t is defined for block t as $\mathcal{M}_t = \{t + 1, \dots, t + M\}$. Subsequently we update the system matrix in (18) to \mathbf{X}_{t+M} using these latest symbol estimates. For clarity we omit the ‘‘hat’’ symbol over \mathbf{X} , even though it generally contains estimated symbols. The Q subsequent estimates $\hat{\mathbf{h}}_{t+M}^q$ for processing block $t + M$ each result from a small number J of iterations of LSQR on (20) for block time $t + M$. Typically in our application, setting J to two or three is sufficient. Invocation of LSQR to estimate $\hat{\mathbf{h}}_{t+M}^q$ requires the system matrix \mathbf{X}_{t+M} , the

observation vector \mathbf{y}_{t+M}^q , and an initial guess for the CIR solution, which we specify as the previous block's CIR estimate $\hat{\mathbf{h}}_t^q$.

For a block, there are Q LSQR invocations iterating J times, each calculating an approximate solution for the q^{th} CIR estimate vector. Thus, for each block DDPPC first performs the LSQR-based CIR estimation step, then the PPC symbol estimation step, advancing through the received data stream by M new samples per block. We find empirically that an update interval size M on the order of the CIR length L is adequate to control modeling error due to channel parameter evolution over the decision delay interval.

The computation cost of an LSQR iteration when used in our application is dominated by matrix-vector multiplies involving \mathbf{X}_t and its transpose, which due to its Toeplitz form can be accomplished efficiently through circulant embedding and FFT vector-matrix multiplies (fast convolution). This results in $\mathcal{O}(JQ(N+L)\log(N+L))$ complexity per block for CIR estimation. Assigning $M \leftarrow L$ as per the discussion above and using the reasonable design rule $N \propto L$ results in a *per-sample* complexity for CIR computation that is sub-linear in the number of observations per block, i.e.,

$$\text{complexity} \sim \mathcal{O}\{J Q \log(N)\}. \quad (21)$$

In our algorithm LSQR is restarted every block by initializing it with the previous block's CIR estimate. This permits rapid convergence of the LSQR solution with a small number of iterations while decoupling estimates between successive blocks, unlike standard RLS. Thus DDPPC avoids committing to a specific correlation model for multipath parameter time-evolution, yet still exploits inter-block CIR correlations for numerical efficiency.

3.2.3 PPC filtering and detection

Here we describe the application of the PPC filtering operations (9) and (10) to the DDPPC adaption scheme. PPC filtering is followed by phase synchronization and symbol detection.

The PPC step associated with CIR estimation block t (20) forms the demodulation r in (9) for M time samples immediately following t . These times constitute the update block interval. Any samples of r prior to the update interval have already been detected and used to populate the symbol matrix \mathbf{X}_t . More precisely, the PPC step at block t calculates $r(\tau)$ using (9) for $\tau \in \mathcal{M}_t$, where $\mathcal{M}_t = \{t+1, \dots, t+M\}$. However, this calculation must use *predicted* CIR values, because the LSE $\hat{\mathbf{h}}_\tau^q$ of (20) is not available (because \mathbf{X}_{t+M} is not yet defined). We employ the simplest possible prediction $\hat{\mathbf{h}}_{\tau|t}^q$ of \mathbf{h}_τ^q by assigning to it the value of the latest computed CIR vector estimate, i.e.,

$$\hat{\mathbf{h}}_{\tau|t}^q \leftarrow \hat{\mathbf{h}}_t^q. \quad (22)$$

The predicted CIR is then correlated with the channel observation $y^q(\cdot)$ so that the calculation of $\hat{r}(\tau)$ is

$$\hat{r}(\tau) = \sum_{q=1}^{N_c} \hat{z}^q(\tau) \quad (23)$$

$$\hat{z}^q(\tau) = \sum_{l=0}^{L-1} \hat{h}_t^{q*}(l) y^q(\tau+l) \quad (24)$$

In addition to the errors \bar{w} appearing in the ideal, fixed-channel PPC demodulation r (12), \hat{r} is also contaminated by components due to CIR estimation error $\mathbf{h}_t^q - \hat{\mathbf{h}}_t^q$ and CIR prediction error $\mathbf{h}_{t+k}^q - \hat{\mathbf{h}}_t^q$. The resulting aggregate error increases with decision delay and relative platform motion. In order to accomplish phase synchronization of \hat{r} prior to detection, we model this error as multiplicative and estimate its systematic components by a straightforward decision-directed method similar to an algorithm in [17]. The (conjugated) phase error estimates then form the phase correction $\hat{\beta}$. Once \hat{r} is corrected with $\hat{\beta}$, memoryless quantization appropriate for the signaling scheme then detects the symbol estimates. For details on estimating $\hat{\beta}$, see [14].

3.2.4 DDPPC Pseudocode

A pseudocode outline of the DDPPC algorithm applied to one packet is shown in Fig. 3.

The algorithm generalizes readily to the fractionally spaced case, where K samples per symbol are required. For the case of linear modulation, we still maintain the baseband-equivalent impulse response model that includes the

```

Define  $\mathcal{M}_t = \{t + 1, \dots, t + M\}$ 
 $t \leftarrow N + L - 1$ 
For each channel  $q$ :
     $\hat{\mathbf{h}}_t^q \leftarrow \operatorname{argmin} \|\mathbf{X}_t \mathbf{h}_t^q - \mathbf{y}_t^q\|^2$ 
    Calc.  $\hat{r}(\tau)$  and  $\hat{I}_\tau$  for all  $\tau \in \mathcal{M}_t$ 
    Init. synchronization parameter  $\hat{\beta}$ 
 $t \leftarrow t + M$ 
While{ more data in packet}
    For each channel  $q$ :
         $\hat{\mathbf{h}}_t^q \leftarrow \operatorname{LSQR}(\mathbf{X}_t, \mathbf{y}_t^q, \hat{\mathbf{h}}_{t-M}^q)$ 
        Calc.  $\hat{r}(\tau)$  and  $\hat{I}_\tau$  for all  $\tau \in \mathcal{M}_t$ 
        Update  $\hat{\beta}$ 
     $t \leftarrow t + M$ 

```

Figure 3: DDPPC pseudocode for 1 packet and MPSK modulation

transmit pulse shape in the CIR. Then \mathbf{X}_t is formed from a stream of symbols that has been zero-filled according to K . K column partitions of \mathbf{X}_t are thus orthogonal, allowing decomposition of the linear model into K separate estimation problems per channel. For the case of non-linear modulation schemes where column orthogonality is not satisfied, the K -wise increase in problem size benefits from the FFT-based fast multiply used by the LSQR iterations.

4 Performance Evaluation

In this section, the DDPPC algorithm is tested using data taken in a recent sea test. The particular data sets used represent three of the more interesting cases encountered during the experiment. After describing the cases, the performance metrics are defined. Algorithm performance is studied using various sub-apertures of the 14-element array ranging from the full aperture to just two elements. Results are quantified in terms of bit error rate, detector input mean squared error, detector input SNR, and processing gain.

4.1 Test Conditions

A proof-of-concept demonstration of the PPC architecture was performed in Puget Sound near Seattle in May 2000. Fig. 4 shows the basic geometry. One or more acoustic sources sent data to a 14-element receiving array. Several experimental parameters were varied. Ranges between 500 m and 5 km were considered, and the water depth varied between 10 and 120 m. The spacing between the elements in the array was adjustable, as was the array shape. The source was either moored, allowed to drift, or fixed to the seabed. Over the course of the one-week experiment, a variety of environmental conditions were encountered. A more complete description of the experiment and the hardware used is in Rouseff *et al.*[12].

The three cases considered in this paper shared certain environmental conditions and also have certain common parameters. CTD casts show the sound speed in the water column to be nearly constant and independent of depth. The receiving array spanned the water column with approximately 2 m spacing between elements. The symbol rate was 2174 Hz, and BPSK signaling was used. The transmit spectrum was centered at approximately 12 kHz and has bandwidth of 13 kHz, as shown in Fig. 5.

The packet length was 10000 symbols plus the additional symbols used for training, and lasted about 4.6 seconds. Fig. 6 shows representative baseband acquisition data as observed at the deepest array element for each of the three cases. Throughout the remainder of the paper, the labels \mathcal{A} , \mathcal{B} , and \mathcal{C} refer to the three experiments' data sets. The particulars of these observations and the three cases are as follows.

Case \mathcal{A} The source was moored 0.9 km from the array. The SNR was high as can be inferred from the top panel in Fig. 6 by comparing the signal level during the data transmission to what was observed before it commenced. The method for quantifying the SNR will be detailed later. Because the range was relatively short and the environment benign, the CIR was quite long for this case. This can be inferred by looking at the response in Fig.

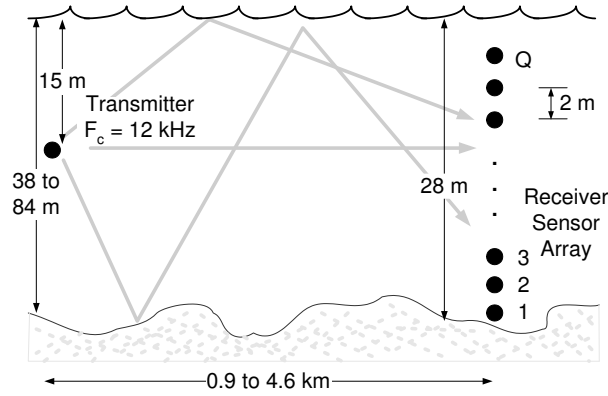


Figure 4: Experiment configuration.

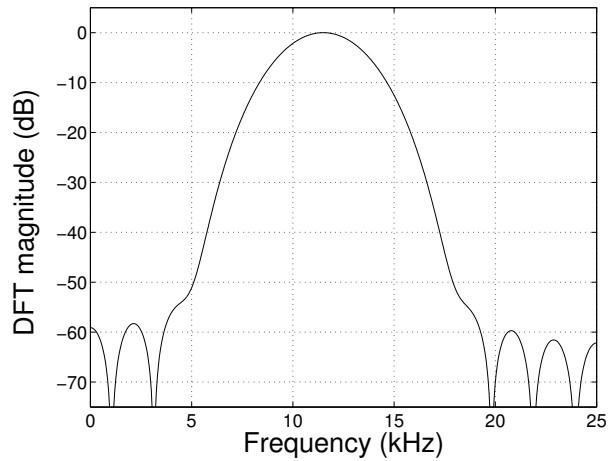


Figure 5: Interpolated DFT magnitude of full-BW transmit pulse used in actual telemetry experiments.

6 after the data transmission has stopped. A full second after the transmission has halted, the received signal has still not returned to the ambient noise level seen before transmission. In the processing, the CIR was modeled as being $L = 108$ symbols in duration, corresponding to a nominal delay spread of approximately 50 ms. Thus we model the remainder of the decaying response “tail” in the top panel of Fig. 6 as reverberation (7). The update interval size was $M = 100$ symbols.

Case B In this case, the source was 3.7 km from the array and unmoored. The source’s drift rate was estimated at 0.5 m/s. An additional complication was the presence of a strong impulsive noise source, probably due to an automobile ferry. The noise spikes are present both before and during transmission as can be observed in the middle panel of Fig. 6. The CIR length L was reduced to 50 symbols, corresponding to a delay spread of 23 ms, and the size of the update interval to 75 symbols.

Case C As in the previous case, the source drifted at 0.5 m/s. The range was increased to 4.6 km. Heavy rain at the time of this test contributing to ambient ambient noise. The truncated response is shown in the bottom panel of Fig. 6. The CIR length L was reduced to 35 symbols, corresponding to a delay spread of approximately 16 ms. The size of the update interval is 50 symbols.

The parameters of the three cases are summarized in Table 2. The table includes the processing parameters N (the number of LSE observations), M (block increment size) and L (CIR length).

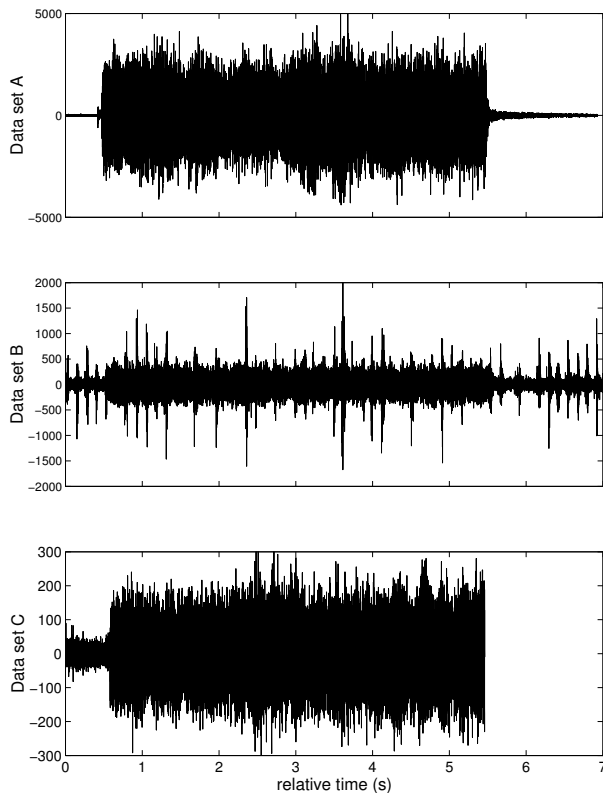


Figure 6: Real component of deepest sensor’s baseband acquisition data (BW=13 kHz) for the three experimental data sets, illustrating noise conditions. Reverberation apparent at end of packet in data set \mathcal{A} . Data set \mathcal{B} contaminated by shipping noise. Data set \mathcal{C} truncated. Amplitude in D/A conversion units.

Additional parameters varied are the number and location of the hydrophone channels used in the processing. As noted earlier, the full array for these three cases spanned the water column and had 14 elements. In the following sections, we evaluate DDPPC using subsets of the full array consisting of from two to 14 contiguous elements. The configurations tested are shown schematically in Fig. 5. The first column is the hydrophone index. Consistent with Fig. 3, the array elements are labeled so that the hydrophone index increases with depth. A “o” character means the element is used in a particular configuration, while a dash means it is not. For example, there are three scenarios where $Q = 7$ hydrophones are used: the first with the bottom seven elements, the second with mid-water elements, the third with the elements nearest the sea surface. Four combinations of four elements were considered, and so on. The telemetry results reported in the following subsections represent averages over the different combinations employed.

4.2 Statistics for Performance and Channel Quality

This section describes metrics used to estimate quality of the communication channel and to measure performance of DDPPC. The presence of multiple error sources in the signal model somewhat complicates the definition, estimation, and interpretation of noise variances and metrics derived from them. To address these issues we discuss signal-to-noise ratios (SNR) that consider ambient noise, reverberation, and other modeling error. We also define noise variances, received energy per symbol \mathcal{E}_s , detector mean square error (MSE), “output” SNR measured at the detector input, processing gain, and bit error rate (BER).

4.2.1 Channel SNR and Noise Variance Definitions

For the wideband experimental data sampled without aliasing, a ratio of received symbol energy to noise spectral density is an inappropriate metric for SNR. This is because the non-flat pulse shape induces a colored reverberation

| $Q :$ | 14 | 7 | 4 | 3 | 2 | | | | | | | | | | | | | | |
|-------|----|---|---|---|---|---|---|---|---|---|---|---|---|---|---|---|---|---|---|
| 14 | o | o | - | - | o | - | - | - | - | o | - | - | - | - | - | - | - | - | - |
| 13 | o | o | - | - | o | - | - | - | - | o | - | - | - | - | - | - | - | - | - |
| 12 | o | o | - | - | o | - | - | - | - | o | o | - | - | - | - | - | - | - | - |
| 11 | o | o | - | - | o | - | - | - | - | o | - | - | - | - | - | - | - | - | - |
| 10 | o | o | o | - | - | o | - | - | - | o | - | - | - | - | - | o | - | - | - |
| 9 | o | o | o | - | - | o | - | - | - | o | - | - | - | - | - | o | - | - | - |
| 8 | o | o | o | - | - | o | - | - | - | o | - | - | - | - | - | o | - | - | - |
| 7 | o | - | o | o | - | o | o | - | - | o | - | - | - | - | - | o | - | - | - |
| 6 | o | - | o | o | - | - | o | - | - | - | o | - | - | - | - | - | - | o | - |
| 5 | o | - | o | o | - | - | o | - | - | - | o | - | - | - | - | - | - | o | - |
| 4 | o | - | o | o | - | - | o | o | - | - | - | o | - | - | - | - | - | - | o |
| 3 | o | - | - | o | - | - | - | o | - | - | - | - | o | - | - | - | - | - | o |
| 2 | o | - | - | o | - | - | - | o | - | - | - | - | o | - | - | - | - | - | o |
| 1 | o | - | - | o | - | - | - | o | - | - | - | - | o | - | - | - | - | - | o |

Figure 7: Hydrophone sets used to test DDPPC algorithm under various number of aperture channels Q . Symbol “o” indicates location of hydrophone enabled in each of the 20 aperture configurations. Each row corresponds to a hydrophone index. Each column corresponds to an aperture configuration.

noise correlation at the downconversion filter output that cannot be reproduced by “equivalent” white channel noise. For this reason we use SNR metrics based on the power ratio $[P_{signal}/P_{noise}]^q$ for sensor q , which is

$$\begin{aligned} \frac{\mathcal{E}_s^q \times (\text{symbol rate})}{\frac{\text{noise energy}}{\text{sample}} \times (\text{samp. rate})} &= \frac{\|\mathbf{h}_t^q\|^2 \Delta T (F_{sym})}{\sigma^2 \Delta T (K F_{sym})} \\ &= \frac{\|\mathbf{h}_t^q\|^2}{K \sigma^2}, \end{aligned} \quad (25)$$

where the processing sample rate is $F_s = \Delta T^{-1} = K F_{sym}$, and σ^2 is variance of a generic noise source for sensor q measured over the sampling bandwidth (i.e., after downconversion filtering). Subject to anti-aliasing constraints, $[P_{signal}/P_{noise}]^q$ is insensitive to the value of K if pulse bandwidth is held constant.

Eqn. (25) uses received energy per symbol \mathcal{E}_s^q in conjunction with the noise variances σ_{amb}^{q2} and σ_{tot}^{q2} (defined later) to form respectively the distinct SNR metrics SNR_{amb}^q and $SINR^q$, so that

$$SNR_{amb}^q = \left[\frac{P_{signal}}{P_{noise}} \right]_{\sigma=\sigma_{amb}^q}^q \quad (26)$$

and

$$SINR^q = \left[\frac{P_{signal}}{P_{noise}} \right]_{\sigma=\sigma_{tot}^q}^q \quad (27)$$

Essentially, SNR_{amb}^q approximates the sensor- q SNR for an isolated pulse before reverberation can fully emerge, whereas $SINR^q$ incorporates unmodeled excess delay spread from reverberation due to previously transmitted symbols.

The metric SNR_{amb}^q uses the parameter σ_{amb}^{q2} , the variance of the noise $v_{amb}^q(\tau)$ in eqn. (4). This noise includes both ambient and receiver thermal noises, and we label it simply *ambient noise*. We denote the noise variance used in $SINR^q$, σ_{tot}^{q2} , as that of *total noise*, which in addition to ambient noise includes interference from the reverberation signal (7) induced by the packet transmission. We model the effect of reverberation as a random process and assume its spectral shape substantially matches that of the transmit signal, based on empirical analysis presented in [23].

Our motivation for considering the metric $SINR^q$ is that the LSE residual-sum-of-squares (RSS) are seen in our experiments to be much higher than can be accounted for by the quiescent estimates of σ_{amb}^{q2} . This suggests that the modeled CIR length L may be too small [20, p. 209]. We interpret the “missing” parameters to be in part an effect of the reverberation which emerges shortly after the beginning of the packet transmission, made explicit in (7). These components of the CIR are likely to be so rapidly varying and numerous that they cannot be estimated, so we aggregate

them into the noise term. Total noise thus is the sum of the two uncorrelated random terms $v_{rev}^q(\tau)$ and $v_{amb}^q(\tau)$ in eqn. (6), so that its variance is

$$\sigma_{tot}^{q2} = \sigma_{amb}^{q2} + \sigma_{rev}^{q2} \quad (28)$$

Note that σ_{tot}^{q2} represents all noise in the channel, but not the total *observation* error (6) of CIR estimation. This is because we consider the time-varying modeling error (TVME) component $v_{tv}^q(t, \tau)$ in (6) to be due to our block-based estimation set-up, and not an intrinsic source of noise in the channel.

4.2.2 Estimating Components of SNR

Here we describe estimation of components used in the channel SNR metrics.

Ambient noise is observed in $y^q(t)$, the downconverter filter output, immediately prior to the reception of a data packet assuming a quiescent environmental state. Assuming stationarity, we calculate its variance estimate $\hat{\sigma}_{amb}^{q2}$ for sensor q by squared sample standard deviation.

To estimate the variance of the channel's total noise $v_{rev}^q(\tau) + v_{amb}^q(\tau)$ for sensor q , we decompose the total CIR LSE observation error variance, σ_v^{q2} in (19), as

$$\sigma_v^{q2} = \sigma_{rev}^{q2} + \sigma_{amb}^{q2} + \sigma_{tv}^{q2} = \sigma_{tot}^{q2} + \sigma_{tv}^{q2}. \quad (29)$$

To solve for σ_{tot}^{q2} we first estimate σ_v^{q2} following common usage of the unbiased estimator for variance of unit weight [20] $RSS_t^q / (N - L)$, where the LS residual-sum-of-squares RSS_t^q for block t and channel q is $\|\mathbf{y}_t^q - \mathbf{X}_t \hat{\mathbf{h}}_t^q\|^2$. Assuming stationarity we average over all blocks t in the packet, giving an estimate of total variance for sensor q as

$$\hat{\sigma}_v^{q2} = \overline{RSS^q} / (N - L). \quad (30)$$

Note that the L and N include oversampling factor K . The unbiased property does not require a Gaussian noise assumption here.

To mitigate the effects of TVME (8) on estimates of channel noise, some measure of its severity must be quantified. Interpreting TVME as being random and uncorrelated with other quantities, we approximate its variance σ_{tv}^{q2} by using a channel propagation simulator developed in [23]. Here the simulator recreates the propagation of wideband transmissions, using an estimate of the model (4). The time-varying CIRs used here are derived from estimates generated by the DDPPC CIR estimation algorithm operating on the original experiment data sets. This procedure includes suitable bandwidth constraints on the time-varying CIR coefficient history. The resulting synthesized observations are then free from channel noise components. Applying the DDPPC CIR estimation structure to the noise-free simulated observations, we estimate the observation error variance from LSE residuals based on the piecewise-invariant CIR model (18), similarly to the estimation of $\hat{\sigma}_v^{q2}$ in eqn. (30). Since in this CIR estimation step the (simulated) observations are free from reverberation and ambient noise, we interpret this estimated variance to be an *ad hoc* estimate of TVME power σ_{tv}^{q2} . We then subtract $\hat{\sigma}_{tv}^{q2}$ from $\hat{\sigma}_v^{q2}$ so that the estimator for variance of total noise in the channel is

$$\hat{\sigma}_{tot}^{q2} = \hat{\sigma}_v^{q2} - \hat{\sigma}_{tv}^{q2}. \quad (31)$$

For more discussion see [23].

Here we discuss estimation of received energy per symbol for sensor q , defined as

$$\mathcal{E}_{s,t}^q = \|\mathbf{h}_t^q\|^2 \Delta T = \|\mathbf{h}_t^q\|^2 (KF_{sym})^{-1} \quad (32)$$

for processing block t . Simply replacing the unknown $\|\mathbf{h}_t^q\|^2$ with $\|\hat{\mathbf{h}}_t^q\|^2$ in (32) produces a biased estimate of $\mathcal{E}_{s,t}^q$. Under the model defined by (18) and (19), the CIR estimate covariance is

$$\text{cov}(\hat{\mathbf{h}}_t^q) = \sigma_v^2 [\mathbf{X}_t' \mathbf{X}_t]^{-1} \quad (33)$$

[20]. Using this fact it is straightforward to show that the bias in the estimate $\|\hat{\mathbf{h}}_t^q\|^2$ is

$$E\|\hat{\mathbf{h}}_t^q\|^2 - \|\mathbf{h}_t^q\|^2 = \sigma_v^2 \text{trace}\{[\mathbf{X}_t' \mathbf{X}_t]^{-1}\}. \quad (34)$$

This motivates use of the following unbiased estimator for the received energy per symbol for sensor q , averaged over all estimation blocks t in the packet:

$$\hat{\mathcal{E}}_s^q = \frac{\Delta T}{\# \text{ blocks}} \sum_t \|\hat{\mathbf{h}}_t^q\|^2 - \hat{\sigma}_v^{q2} \text{trace}\{[\mathbf{X}_t' \mathbf{X}_t]^{-1}\} \quad (35)$$

Using the definitions above, eqns. (26) and (27) give estimates of SNR_{amb}^q and $SINR^q$, respectively. These sensor-specific metrics are then averaged over all Q sensors in the aperture to give the average-per-sensor SNR metrics SNR_{amb} and $SINR$. For notational simplicity we omit the “hat” symbol over the SNR metrics.

4.2.3 DDPPC Performance Metrics

Here we define metrics used to evaluate performance of the DDPPC algorithm.

To measure combined ISI and noise in the decision metric $\hat{r}(\tau)$ we use mean squared error (MSE), calculated as the sample variance of $\hat{r}(\tau)I_\tau^*$ after normalization by its sample mean.

We use a measure of SNR at the DDPPC soft demodulation $\hat{r}(\tau)$ to study the coherent processing gain achieved prior to symbol detection. This metric, denoted SNR_{out} , should aid evaluation of concatenated systems where the DDPPC algorithm is followed by another single channel equalizer or sequence detector operating on the signal $\hat{r}(\tau)$. Assuming symbol rate sampling of \hat{r} by the detector (implying decimation if $K > 1$ in upstream processing), we define SNR_{out} to measure SNR at the detector input, so that

$$SNR_{out} = \mathcal{E}_d / \sigma_d^2, \quad (36)$$

where \mathcal{E}_d and σ_d^2 are the symbol energy and noise variance respectively seen at the detector input. These quantities represent an interpretation of the DDPPC processing up to the detector input as a “virtual channel” having a single input (I_k) and a single output (\hat{r}). We estimate the components \mathcal{E}_d and σ_d^2 of SNR_{out} following the methods described above for estimating \mathcal{E}_s^q and σ_v^{q2} . Here statistics are derived from off-line LS identification of the total impulse response $\bar{\rho}_k$ in (12), similarly to the procedure outlined in Section 3.2.1. Under this estimation set-up, the length of the total CIR $\bar{\rho}_k$ is modeled as $2L - 1$, \mathcal{E}_d is the squared norm of $\bar{\rho}_k$, and σ_d^2 is the variance of \bar{w} . Note that σ_d^2 does *not* exclude the effects of the TVME error components present at the detector input, in contrast to the case for estimating individual channel noise variances σ_{tot}^{q2} . We justify this difference by reasoning that once the PPC filtering and combining operation is performed using estimated CIRs, the contamination of the detector input signal due to CIR estimation errors is not likely to be reversible in practice; thus the error \bar{w} at that point should be considered to be noise intrinsic to the algorithm’s interpretation as a virtual channel. For simplicity we assume \bar{w} to be stationary and white. The metric SNR_{out} differs from the MSE metric in that it considers the components seen as ISI by MSE to be part of the signal, rather than interference.

Given $SINR$ and SNR_{out} , processing gain G of DDPPC at the detector input is the ratio $SNR_{out}/SINR$.

Empirical bit error-rate (BER) is the fraction of incorrectly detected bits to the total number of bits detected during a test.

4.3 DDPPC performance on experimental telemetry data

Results from DDPPC demodulation of the packets transmitted during the telemetry experiments is shown here using the full transmit pulse bandwidth of 13 kHz for various aperture configurations.

Since the experimental transmit pulse bandwidth is approximately six times the symbol rate F_{sym} , a straightforward fractionally-spaced generalization of the DDPPC algorithm is employed where estimation, phase synchronization, and PPC filtering are performed at sample rate $F_s = KF_{sym}$ with $K = 6$. Performance results of the DDPPC algorithm on the full-bandwidth signal are shown in Table 3. Downconversion filtering effectively suppresses energy outside the 13 kHz signal bandwidth and is flat inside the signal spectrum. Performance metrics are shown with several aperture sizes up to the full aperture of $Q = 14$. When $Q < 14$, results shown in Table 3 are averages taken over all subaperture positions, conditioned on the given value of Q . A single 10000-bit packet realization is used for all aperture evaluations.

We report results for $J = 2$, where J is the number of LSQR iterations used for each sensor’s CIR estimate computation. Under low-BER conditions, the empirical BER approximately doubles when reducing the number of iterations from two down to one, and is reduced by approximately 10% by using five iterations. At higher BER

conditions (e.g. with reduced spatial apertures), the reduction in BER attained by going from two to five iterations is not clearly discernable. Thus for these shallow-water conditions, choosing two LSQR iterations seems economical. However, for purposes of estimating the input SNR levels, five LSQR iterations are used.

In our evaluation, the parameters N , M , and L are set by cursory examination of preliminary channel estimates and the algorithm's behavior. Increasing N will reduce error in CIR estimation due to reverberation and ambient noise, but will increase estimation error and CIR prediction error due to TVME in (6). Increasing M makes the algorithm more efficient computationally, but increases CIR prediction error and error in the phase synchronization parameter $\hat{\beta}$. Increasing L might reduce estimation error due to reverberation, but will increase errors due to ambient noise. The parameter values we use are not necessarily optimal, and automating their specification is a topic beyond the scope of this paper.

A byproduct of the DDPPC is a set of evolving estimates of the baseband channel scattering during the packet, which can be interpreted as a time-varying delay-spread function. The modulus of these estimates for the deepest hydrophone of the three data sets are shown in Fig. 8, produced by DDPPC operating on the full bandwidth, full aperture telemetry data. Here the extent of the delay spread and its fading behavior is apparent. The tracking ability of the fixed-size, uniformly weighted estimation window of DDPPC is demonstrated further by the rapid drift in the channel's bulk time delay shown in the datasets \mathcal{B} and \mathcal{C} . This shows that even with simple fixed frame synchronization (done at the beginning of the packet and not adapted continuously), DDPPC still tracks the CIR effectively during packets of almost five seconds in duration. Transients apparent during some blocks in the CIR estimates for data set \mathcal{B} are due to a highly impulsive shipping noise source.

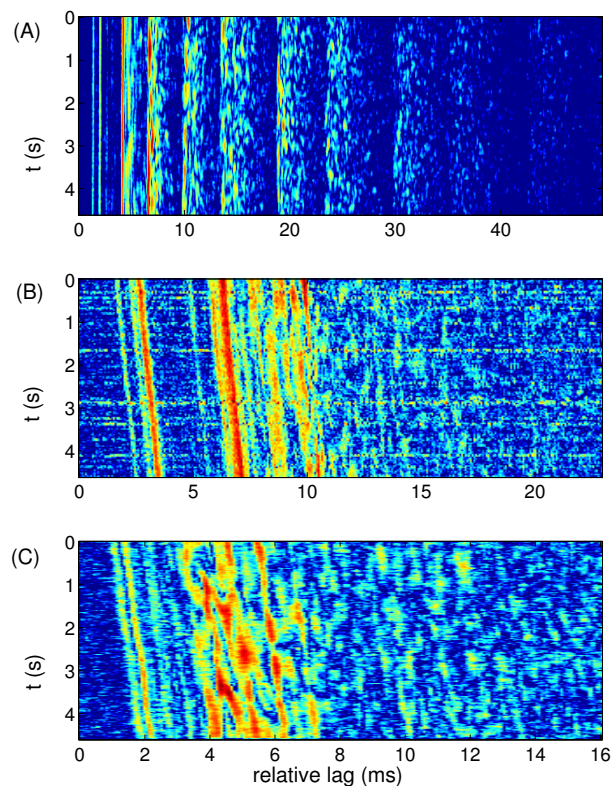


Figure 8: Evolving CIR estimates produced by DDPPC algorithm with full bandwidth and fractional processing at $6 \times$ the symbol rate. Result for deepest array element. Vertical axis is block time t , and horizontal axis corresponds to impulse response lag variable l . A horizontal slice of an image represents the vector $|\hat{\mathbf{h}}_t^q|$. Intensity scales all have 24 dB dynamic range. (A) - Data set \mathcal{A} ; (B) - Data set \mathcal{B} ; (C) - Data set \mathcal{C} .

The tests results using a reduced number of receiver hydrophones suggest that a full aperture spanning the water column is not required to realize good equalization performance from the PPC method under these conditions, although performance improves with the number of aperture channels Q . This seems reasonable since as the array becomes

more populated (assuming adequate sensor separation), the number of “independent” autocorrelation lags comprising the summation in (12) increases. This improves ISI suppression relative to the zero-lag peak of $\bar{\rho}_l$.

The gain metric $G = SNR_{out}/SINR$ shows, as expected, more improvement as the number of sensors is increased. Data set \mathcal{A} show an increase in gain of 6.3 dB going from two to 14 sensors, while set \mathcal{B} shows an increase of 3.0 dB and set \mathcal{C} , 4.2 dB. The largest absolute gain achieved by DDPPC is for experiment \mathcal{B} , which is 9.8 dB at full aperture, while the lowest is 3.0 dB for data set \mathcal{A} . This is consistent with SNR_{amb} being highest for \mathcal{A} but lowest for \mathcal{B} , and the premise that the reverberation spectrum mimics the transmit spectrum. Under this assumption, the ability of linear filtering to provide gain against reverberation noise is diminished. Since reverberation dominates ambient noise in data \mathcal{A} , linear processing would not be expected to effectively mitigate its effects. Another result, perhaps alarming at first glance, is that DDPPC gain is negative for smaller apertures applied to \mathcal{A} . Thus the cost of processing incurs noise amplification, as for zero-forcing equalizer algorithms [17], even though no explicit deconvolution is attempted by the PPC filtering process. The fact that experiment \mathcal{A} exhibits the highest SNR suggests that a performance floor in terms of gain vs. SNR is a characteristic of the PPC algorithm. In fact, simulations do bear this out [23]. Nonetheless, DDPPC operating on \mathcal{A} maintains the lowest MSE of the three data sets, and shows the best BER and SNR_{out} .

To illustrate the stability of DDPPC’s tracking capability under various error rates, we show a measure of cumulative BER as a function of time for data set \mathcal{C} . This is shown in Fig. 9 for the different aperture configurations. Here each curve at a given time t is the total number of bit errors up to t , divided by t . The curves for the reduced aperture cases demonstrate that DDPPC can operate at BER levels above 0.01, which is likely to be worse than desired for most error-correcting code designs. Thus we argue that DDPPC is robust to decision errors, enough so that it would not be a source of packet loss.

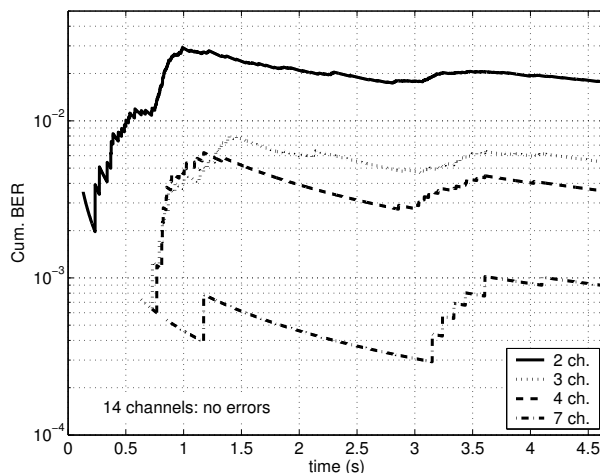


Figure 9: Cumulative empirical BER for the DDPPC algorithm under different aperture subsets. Contiguous sets of sensors are used, each including the deepest sensor. DDPPC shows tracking robustness at BER levels beyond typical levels required for communications. Data set \mathcal{C} .

5 Conclusion

We present the algorithm DDPPC, an adaptive extension to passive phase conjugation [12] array equalization employing a robust decision-directed channel estimation technique. We demonstrate its effectiveness in a shallow-water acoustic modem link that employs a vertical receiver aperture. Performance results on shallow-water experimental telemetry data are shown with ranges of up to 4.6 km, surface winds to 16 m/s, and low relative platform motion. Tests with a reduced number of receiver hydrophones suggest that a full aperture spanning the water column is not necessarily needed to realize good equalization performance from the PPC method. The DDPPC method performed with good uncoded BER at larger apertures and tracks the acoustic channel evolution with excellent compliance in noisy, rapidly-varying environments. The algorithm’s pre-quantized demodulator output can be processed with conventional single-channel equalizers for reduction of residual ISI.

The small number of errors detected during larger apertures suggests that, in order to completely map the performance limits of DDPPC, test conditions need to be more challenging. To this end, we present in the companion paper [24] a simulation method which evaluates DDPPC for these channels at various bandwidths, bit rates, and transmit power levels.

6 Acknowledgment

Darrell Jackson, Chris Jones, and David Dowling participated in the original field experiment demonstrating Passive Phase Conjugation. Dr. Jackson also contributed many useful comments on a preliminary version of this paper. This work was supported by the Office of Naval Research.

References

- [1] M. Stojanovic, J. A. Catipovic, and J. G. Proakis, "Phase-coherent communications for underwater acoustic channels," *IEEE Journal of Oceanic Engineering*, vol. 19, no. 1, pp. 100–111, January 1994.
- [2] M. Stojanovic, "Recent advances in high-speed underwater acoustic communication," *IEEE Journal of Oceanic Engineering*, vol. 21, no. 2, pp. 125–136, April 1996.
- [3] T. H. Eggen, A. B. Baggeroer, and J. C. Preisig, "Communication over Doppler spread channels. Part I: Channel and receiver presentation," *IEEE Journal of Oceanic Engineering*, vol. 25, pp. 62–71, January 2000.
- [4] D. R. Dowling, "Acoustic pulse compression by passive phase-conjugation," *Journal of the Acoustical Society of America*, vol. 95, pp. 1450–1458, 1994.
- [5] D. B. Kilfoyle and A. B. Baggeroer, "The state of the art in underwater acoustic telemetry," *IEEE Journal of Oceanic Engineering*, vol. 25, no. 1, pp. 4–27, January 2000.
- [6] D. R. Jackson and D. R. Dowling, "Phase conjugation in underwater acoustics," *Journal of the Acoustical Society of America*, vol. 89, pp. 171–181, 1991.
- [7] W. A. Kuperman, W. S. Hodgkiss, H. C. Song, T. Akal, C. Ferla, and D. R. Jackson, "Phase conjugation in the ocean: Experimental demonstration of an acoustic time-reversal mirror," *Journal of the Acoustical Society of America*, vol. 103, pp. 25–40, 1998.
- [8] A. Silva, S. Jesus, J. Gomes, and V. Barroso, "Underwater acoustic communication using a 'virtual' electronic time-reversal mirror approach," in *Proceedings of the Fifth European Conference on Underwater Acoustics (ECUA)*, Lyon, France, 2000, pp. 531–536.
- [9] C. Athanasiou, "Comparison of alternate methods of environmentally adaptive underwater acoustic communication systems," Masters thesis in engineering acoustics, Naval Postgraduate School, Monterey, CA, USA, June 2001.
- [10] M. B. Porter, V. K. McDonald, P. A. Baxley, and J. A. Rice, "SignalEx: linking environmental acoustics with the signaling schemes," in *OCEANS 2000 MTS/IEEE Conference and Exhibition, Volume: 1*. 2000, vol. 1, pp. 595–600, IEEE.
- [11] P. Hursky, M. B. Porter, J. A. Rice, and V. K. McDonald, "Passive phase-conjugate signaling using pulse-position modulation," in *OCEANS 2001 MTS/IEEE Conference and Exhibition, Volume: 4*. 2001, vol. 4, pp. 2244–2249, IEEE.
- [12] D. Rouseff, D. R. Jackson, W. L. J. Fox, C. D. Jones, J. A. Ritcey, and D. R. Dowling, "Underwater acoustic communication by passive phase conjugation: Theory and experimental results," *IEEE Journal of Oceanic Engineering*, vol. 26, no. 4, pp. 821–831, October 2001.
- [13] J. A. Flynn, J. A. Ritcey, W. L. J. Fox, D. R. Jackson, and D. Rouseff, "Decision-directed passive phase conjugation: equalisation performance in shallow water," *Electronics Letters*, vol. 37, no. 25, pp. 1551–1552, December 2001.

- [14] J. A. Flynn, J. A. Ritcey, W. L. J. Fox, D. R. Jackson, and D. Rouseff, "Decision-directed passive phase conjugation for underwater acoustic communication with results from a shallow-water trial," in *Conference Record of the Thirty-Fifth Asilomar Conference on Signals, Systems and Computers*. 2001, vol. 2, pp. 1420–1427, IEEE.
- [15] C. C. Paige and M. A. Saunders, "LSQR: An algorithm for sparse linear equations and sparse least squares," *ACM Transactions on Mathematical Software*, vol. 8, no. 1, pp. 43–71, March 1982.
- [16] B. S. Sharif, D. Thompson, J. A. Neasham, O. R. Hinton, , and A. E. Adams, "Performance of an adaptive multichannel combiner for long range underwater communications," *Electronics Letters*, vol. 32, no. 3, pp. 182–183, February 1 1996.
- [17] J. G. Proakis, *Digital Communications*, McGraw–Hill, 3rd edition, 1995.
- [18] H-N Lee and G. J. Pottie, "Fast adaptive equalization/diversity combining for time-varying dispersive channels," *IEEE Transactions on Communications*, vol. 46, no. 9, pp. 1146–1162, September 1998.
- [19] H. Liu, *Signal Processing Applications in CDMA Communications*, Artech House, Inc., 2000.
- [20] K. R. Koch, *Parameter Estimation and Hypothesis Testing in Linear Models*, Springer–Verlag, english edition, 1988.
- [21] H. Meyr, M. Moeneclaey, and S. A. Fechtel, *Digital Communications Receivers*, Wiley, 1997.
- [22] G. A. F. Seber, *Linear Regression Analysis*, John Wiley & Sons, 1977.
- [23] J. A. Flynn, J. A. Ritcey, W. L. J. Fox, and D. Rouseff, "Performance Predictions of Acoustic Communication by Decision–Directed Passive Phase Conjugation," *IEEE Journal of Oceanic Engineering*, Submitted.
- [24] J. A. Flynn, "Array receiver architectures for channels with large delay–Doppler spreading, and application to underwater acoustic communications," Ph.d. dissertation, University of Washington, Seattle, WA, USA, 2003, In preparation.

Table 1: Glossary of principal variables.

| | |
|---------------------|-----------------------------------------------|
| F_{sym} | symbol rate |
| F_s | processor sample rate |
| K | processor oversampling factor = F_s/F_{sym} |
| L | modeled length of CIR |
| M | update increment |
| N | # of estimation observations |
| Q | # sensor channels |
| q | sensor channel index |
| I_k | transmit data symbols |
| f_k | sampled transmit pulse |
| $x(t)$ | transmit waveform |
| $h^q(\tau, l)$ | time-varying CIR |
| $h_t^q(l)$ | fixed CIR, lag l at block t |
| v_{amb}^q | environment + sensor noise |
| v^q | total channel noise |
| $y^q(t)$ | q^{th} sensor received waveform |
| $z^q(t)$ | matched filter output |
| β | phase sync. parameter |
| $r(t)$ | PPC decision metric |
| $\bar{\rho}_t$ | total CIR at detector input |
| \bar{w} | error at detector input |
| \mathbf{y}_t^q | observation vector at block t |
| \mathbf{h}_t^q | CIR vector at block t |
| \mathbf{X}_t | estimator equation model matrix |
| J | # LSQR iterations |
| σ_{amb}^{q2} | ambient noise variance |
| σ_{rev}^{q2} | reverberation power |
| σ_v^{q2} | CIR estimator equation error variance |
| σ_{tot}^{q2} | total channel noise variance |
| \mathcal{E}_s^q | received energy/symbol |
| SNR_{amb} | SNR w.r.t ambient noise |
| $SINR$ | total SNR |

Table 2: DDPPC parameters and conditions of telemetry experiments. Receive array is stationary. (A) data set \mathcal{A} ; (B) data set \mathcal{B} ; (C) data set \mathcal{C} .

| Data set: | \mathcal{A} | \mathcal{B} | \mathcal{C} |
|-------------------------------|---------------|---------------|---------------|
| N (symbols) | 200 | 150 | 100 |
| L (symbols) | 108 | 50 | 35 |
| M (symbols) | 100 | 75 | 50 |
| # training sym. | 307 | 199 | 134 |
| range (km) | 0.9 | 3.7 | 4.6 |
| source depth (m) | 15 | 15 | 15 |
| water depth _{tx} (m) | 38 | 79 | 84 |
| water depth _{rx} (m) | 26 | 28 | 28 |
| wind (m/s) | 8-9 | 10-13 | up to 16 |
| TX speed (m/s) | ~ 0 | 0.5 | 0.5 |

Table 3: DDPPC performance on experimental telemetry of a 10000-bit packet with 13 kHz BW pulse and BPSK signaling at 2174 bps. Performance metrics are conditioned on aperture size Q , and averaged over aperture position. $SINR$ and SNR_{amb} are averages over the entire aperture size of $Q = 14$. BER value of \emptyset indicates no errors observed.

| Data set: | \mathcal{A} | \mathcal{B} | \mathcal{C} | |
|------------------|------------------|----------------------|---------------|-------------|
| SNR_{amb} (dB) | 38.5 | 4.7 | 14.0 | |
| $SINR$ (dB) | 19.1 | 2.7 | 5.7 | |
| $Q=14$ | SNR_{out} (dB) | 22.1 | 12.5 | 14.2 |
| | Gain G (dB) | 3.0 | 9.8 | 8.5 |
| | MSE (dB) | -13.4 | -9.2 | -9.7 |
| | BER | \emptyset | \emptyset | \emptyset |
| $Q=7$ | SNR_{out} (dB) | 19.9 | 11.8 | 13.0 |
| | Gain G (dB) | 0.8 | 9.1 | 7.3 |
| | MSE (dB) | -10.5 | -7.6 | -7.6 |
| | BER | \emptyset | 0.0003 | 0.0003 |
| $Q=4$ | SNR_{out} (dB) | 18.1 | 11.1 | 11.9 |
| | Gain G (dB) | -1.0 | 8.4 | 6.2 |
| | MSE (dB) | -8.3 | -6.2 | -5.9 |
| | BER | 7.5×10^{-5} | 0.0014 | 0.0018 |
| $Q=3$ | SNR_{out} (dB) | 17.5 | 10.4 | 11.0 |
| | Gain G (dB) | -1.6 | 7.7 | 5.3 |
| | MSE (dB) | -7.3 | -5.0 | -5.1 |
| | BER | 0.00068 | 0.0043 | 0.0045 |
| $Q=2$ | SNR_{out} (dB) | 15.8 | 9.5 | 10.0 |
| | Gain G (dB) | -3.3 | 6.8 | 4.3 |
| | MSE (dB) | -5.5 | -3.7 | -3.6 |
| | BER | 0.0043 | 0.011 | 0.013 |